Investigation on thermal conductivity of silver-based porous materials by finite difference method

Ziming Xiong, Xuhui Wang, Mu He, Lahouari Benabou, Zhiqiang Feng

Investigation on thermal conductivity of silver-based porous materials by finite difference method

Ziming Xiong[a †], Xudong Wang[b †], Mu He[*c], Lahouari Benabou[b], and Zhiqiang Feng[a,d]

[a]LMEE Univ-Evry, Université Paris-Saclay, 91020 Evry, France
[b]UVSQ, Laboratoire d'Ingénierie des Systèmes de Versailles, Université Paris-Saclay, 78140, Vélizy-Villacoublay, France
[c]School of Mechanical Science and Engineering, Huazhong University of Science and Technology, 430074 Wuhan, China
[d]School of Mechanics and Engineering, Southwest Jiaotong University, 610031 Chengdu, China

October 31, 2022

Abstract

Porous materials are widely used in the electronics industry and biomedical fields, where sintered silver, as an emerging representative of porous media, is a promising chip-connection material for adoption in third-generation power electronics. One of the important parameters to characterize the heat conduction capacity of porous sintered silver is the thermal conductivity. In this paper, a numerical model for calculating the equivalent thermal conductivity of porous silver is proposed, based on a voxelized mesh, using finite difference method (FDM) instead of the commonly used finite element method (FEM). Comparisons between the two methods are carried out for the classical unit cells such as simple cubic, body-centered cubic, and face-centered cubic, as well as the silver-based stochastic model. The developed finite difference algorithm is valid, and consistent results are obtained.

Keywords: Equivalent thermal conductivity, Finite difference method, Voxelization, Porous media, Sintered silver

1 Introduction

With the widespread use of porous media in the electronics industry and biomedical fields, determining the equivalent thermal conductivity (ETC) of porous media is critical for the proper design of industrial equipment which can be subjected to severe thermal loading during service. In general, there are two ways for estimating the ETC of a material: analytical methods and numerical methods. Analytical methods consist of the formulas proposed by Voigt [1] and Reuss [2]. They determine the upper and lower bounds of a material's ETC. Hashin and Shtrikman [3] used the variational theorem to derive bounds on the ETC of macroscopically homogeneous and isotropic two-phase materials. Other scholars have investigated and predicted the thermal conductivity of porous media using various models or direct estimating techniques, including Maxwell model [4] and Maxwell-Eucken model [5], etc. For other related models, a review is presented by Pietrak et al. [6].

Due to the limits of analytical methods for materials with complex microstructure and morphology, such as nanostructured materials or some advanced composites, useful estimations of effective properties are not achievable. As a result, numerical approaches are very helpful for acquiring appropriate thermal properties. The finite element (FE) approach is a frequently used numerical method for analyzing porous materials on different scales in order to obtain useful equivalent properties. For example, El Moumen et al. [7] calculated

*Correspondence: muhe@hust.edu.cn , mu.he@foxmail.com †These authors contributed equally to this work.

the ETC of porous materials at the microscopic scale using numerical homogenization techniques and morphological analysis. Florez et al. [8] investigated sintered porous media's ETC. They demonstrated that the geometry of the solid matrix in a porous medium has a relevant effect. Signor et al. [9] studied the thermal conductivity with the change of porosity for sintered silver by using finite element analysis in a realistic 3D microstructure. Qing et al. [10, 11] proposed a quantitative technique for evaluating the influence of crack evolution on the ETC of porous sintered silver, and also proposed a numerical approach based on specific microstructural features to calculate the ETC by taking into account the aging response.

Compared to the high usage of the finite element method (FEM), few people use finite difference method (FDM) in combination with the numerical homogenization (NH) method to calculate the ETC. Abudull and E [12] can be considered as pioneers in this field by developing the finite difference heterogeneous multiscale method (FD-HMM) for solving multiscale parabolic problems. The method is based on the heterogeneous multiscale method (HMM) and heterogeneous discretization, specifically focused on fine scales representing the size of tiny regions in the spatial domain. FD-HMM consists of two parts: a macroscopic solution generated on a coarse grid using the known data extracted from the microscopic model solution, and a microscopic solution that is solved from the original equations over a sparse (heterogeneous) spatial domain. Chen et al. [13, 14] used FD-HMM to handle the issues associated with unsaturated water flow in random porous material and later improved the FD-HMM scheme to simulate not only steady saturated flow problems in geostatistical stochastic porous media, but also transient saturated flow problems.

Support operator method (SOM), regarded as one of the most powerful tools in solving anisotropic diffusion problems within the framework of finite difference methods, is also known as the mimetic finite difference method (MFDM). It was developed by Shashkov and Steinberg [15, 16], and they constructed discrete analogs of invariant differential operators like the divergence and gradient. With this method, operators must satisfy discrete analogs of the integral identities that associate the differential operators with their adjoints. Hyman et al.[17] incorporated the boundary conditions (Dirichlet, Neumann, and Robin conditions) into the MFDM on non-smooth logical rectangular grids. Morel et al. [18, 19, 20] used the MFDM to derive a cell-centered diffusion differencing scheme that gives a sparse matrix representation. In contrast, the traditional method of support operators gives a dense matrix representation. Günter et al. [21] offered two discretization techniques (asymmetric and symmetric schemes) on rectangular grids that employ the FDM and SOM conditions. They take a cautious approach by discretizing fluxes on the dual mesh. Thanks to Günter's model, several researchers [22, 23, 24, 25, 26] have studied the thermal diffusion problem in magnetized plasma.

As low-temperature sintering of silver nanoparticles is becoming a reliable technology for solder die attachment of electronic and optical components [27], it becomes necessary to develop numerical approaches with the ability to predict correctly the thermal performance of such materials. Fig.1 illustrates an example of sintered microstructure exhibiting a porous silver network and serving as a joint for heat dissipation between the active component and its substrate. The present paper extrapolates the Günter's two-dimensional model to a three-dimensional model and achieves numerical homogenization for the equivalent thermal conductivity of low-temperature sintered silver particles by using C++ routines. The paper is organized as follows. Section 2 presents the construction of the theoretical model. Section 3 is dedicated to the numerical FDM-based discretization of the 3D theoretical formulation. Section 4 illustrates the numerical solutions for some cases, then conducts some analyses and compares the results with the finite element solutions solved by Comsol. Section 5 studies three kinds of silver-based stochastic porous structures by numerical calculations. Finally, conclusions are drawn in Section 6. The developed FD algorithm in the paper can treat a series of geometrical configurations and has the advantages of (i) eliminating the computational time in the mesh generation, (ii) parallelizing the calculations easily and naturally. The FD algorithm also has a good anti-sawtooth ability and can get rid of the constraint of the interface between different material phases.

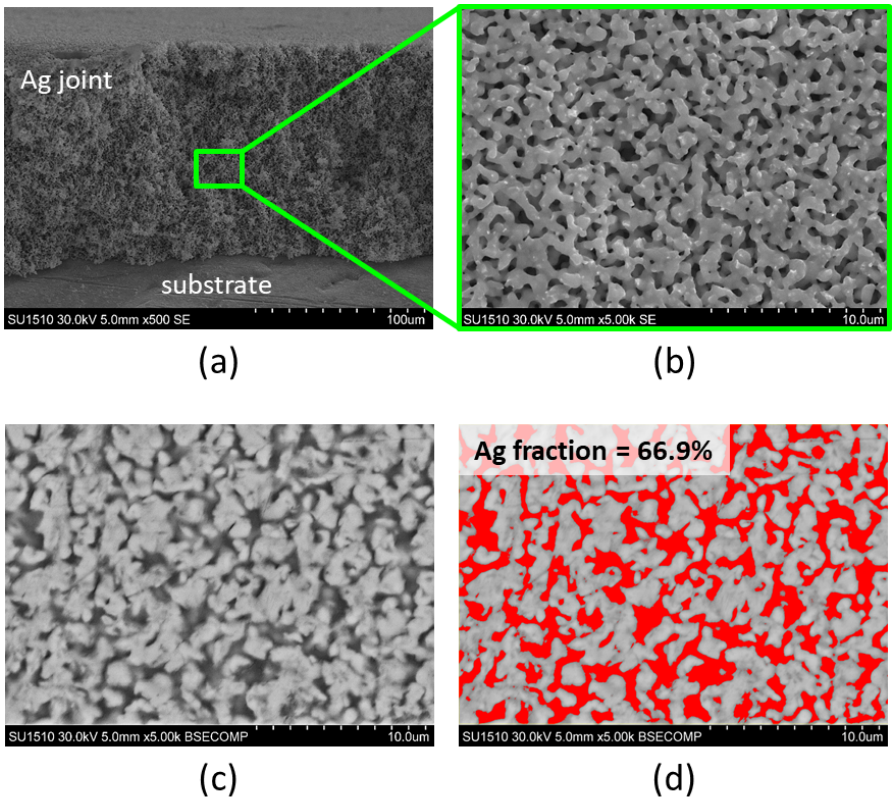

Figure 1: Microscopy of a sintered silver joint after delamination: (a)-(b) global view of the sintered Ag layer and magnified view of the porous silver microstructure, (c)-(d) cross-section of the material and image processing for evaluation of Ag volume fraction

2 Construction of the theoretical model

2.1 Geometrical model

Based on the described background, we consider for the sake of simplicity three typical types of lattice structures: simple cubic crystal form (SC), body-centered cubic crystal form (BCC), and face-centered cubic crystal form (FCC), and their conjugated structures. The theoretical geometric models are shown in Fig. 2, where the spherical particles in Fig. 2a-c can represent either atomic/molecular clusters at mesoscopic scale, or stacked granules at the macroscopic scale. The spheres keep in touch or overlap with each other (marked in color) to meet practical situations: for example, in a mechanical system with large number of loose particles, they are deformed due to squeezing actions and therefore form contact surfaces; in a heat transfer system, the clusters of sintered silver will fuse together and penetrate into each other with the increase of sintering time, and the porosity of the overall structure reduces as the overlap area increases. Consequently, the use of these simple basic models can provide references for complex structures. In our case, these ideal arrangements of particles offer good approximations for real powder compacts prepared by sintering and serve to illustrate different packing factors of the particles with more or less porous silver particle networks [27].

It is noted that the ideal geometrical models that we considered possess the property of spatial periodicity. The representative cell can be obtained by cutting out along the orthogonal edges illustrated in Fig.2d-f. In the subsequent study, the side length of the cell is taken to be the unit length $L_{SC} = L_{BCC} = L_{FCC} = 1$. They are composed of two phases: a solid part consisting of silver contacting balls and a remaining void part filled with air. To calculate the equivalent thermal conductivity under normal conditions, it is necessary to ensure that the solid phases are connected as a single entity. However, considering only the solid phases will lead to the porosity of the studied structures varying only within a small range. Hence, in order to verify the robustness of our developed algorithm, their conjugated structure are also considered (see Fig. 2g-i), i.e., the gas phase and solid phase are swapped to obtain a broader range of porosity.

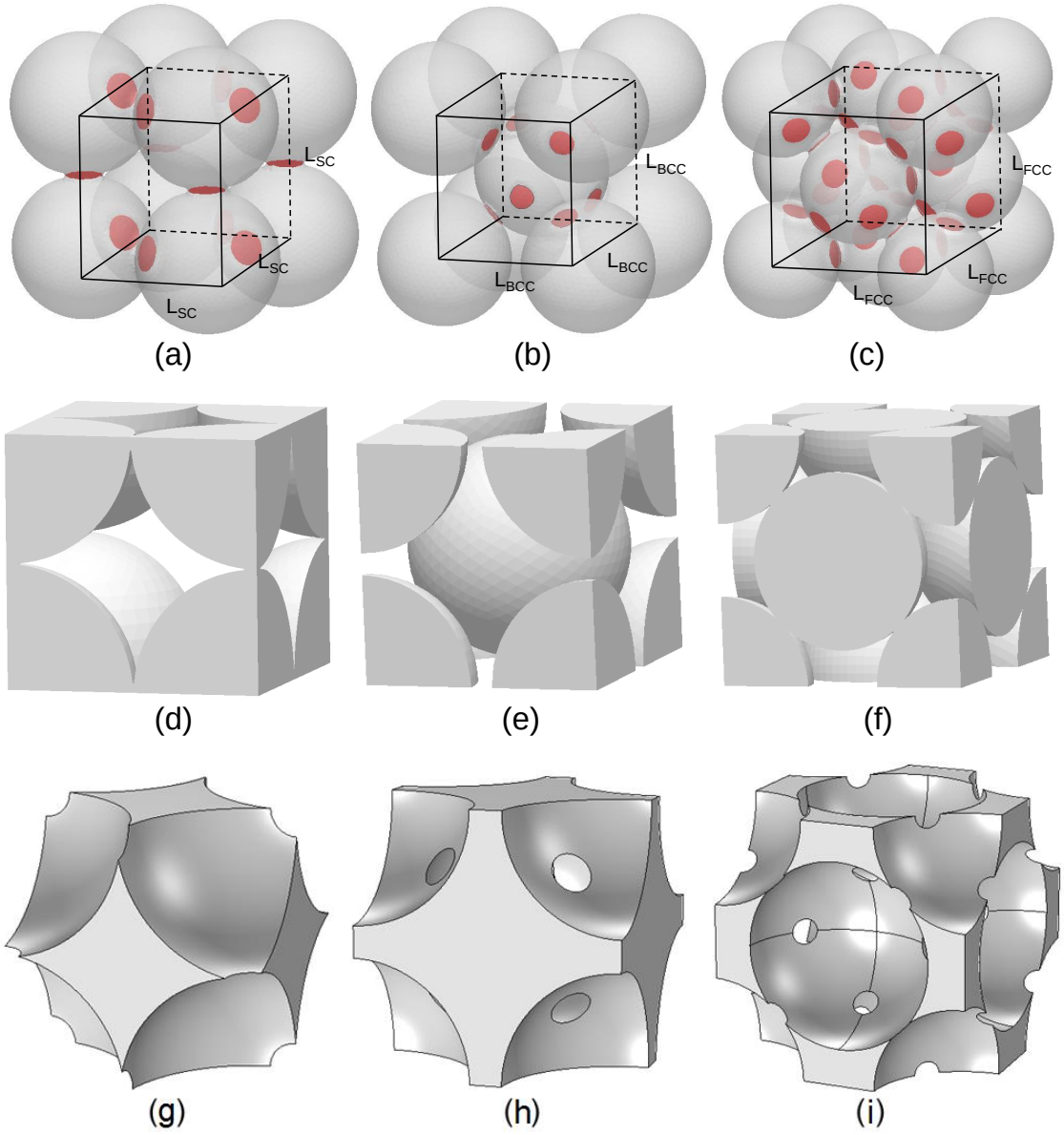

Figure 2: Illustration of geometrical models considered: (a)-(c) structures of simple cubic (SC), body-centered cubic (BCC) and face-centered cubic (FCC), the colored parts indicate the overlaps; (d)-(f) the corresponding periodical unit cells; (g)-(i) the corresponding conjugated structure models.

2.2 Physical model

We investigate the equivalent thermal conductivity of the proposed structures and let $\Omega = [0, 1]^3$ be the domain of interest. The Ω should satisfy the general anisotropic thermal diffusion phenomenon, which is described by the following equations:

$$\overrightarrow{q} = -D \cdot \nabla T, \quad \frac{\partial T}{\partial t} = -\nabla \cdot \overrightarrow{q} + f \tag{1}$$

where T represents the temperature field, D the thermal conductivity tensor of 2^{nd} order, $\overrightarrow{q}$ the heat flux, ∇ the spatial derivative operator and f is the source term. For an isotropic case, the conductivity tensor D is independent of directions and can be reduced to a scalar k.

In this research, we focus mainly on steady-state conditions, and no source term is taken into account such that:

$$\nabla \cdot \overrightarrow{q} = 0 \tag{2}$$

The thermal problem should be completed by adding boundary conditions (BCs) to make the equations solvable. Under typical situations, the BCs prescribe the boundary's temperature and/or flux, such that:

$$\begin{aligned} T &= T_0 \quad on \quad \partial\Omega_{(T)} \\ \overrightarrow{q} \cdot \overrightarrow{n} &= q_0 \quad on \quad \partial\Omega_{(q)} \end{aligned} \tag{3}$$

where $\partial\Omega$ denotes the boundary of Ω, $\overrightarrow{n}$ the normal unit vector to the boundary, T_0 and q_0 are the temperature and heat flux on $\partial\Omega_{(T)}$ and $\partial\Omega_{(q)}$, respectively.

Following this physical model, a computational scheme based on the mimetic finite difference method (FDM) is developed in the next section and then compared with the traditional finite element method (FEM).

3 Numerical discretization for 3D formulation

3.1 Development of finite difference scheme based on the voxel grid

The finite difference scheme we used is based on the theory proposed by Günter et al. [21]. We extend it from 2D to 3D case and apply it to problems of thermal homogenization. The theory's main idea indicates that a symmetric system is constructed in this scheme, where the duality and self-adjointness of differential operators are maintained for the mimetic finite difference method. We will gradually display this framework and derive each term in the thermal diffusion formula.

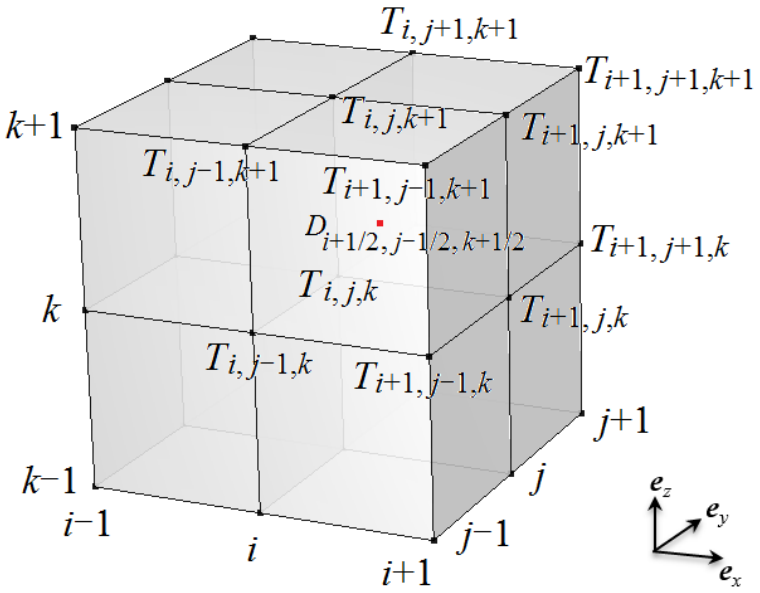

Figure 3: Illustration of the 3D finite difference scheme based on voxel grid

First, a cartesian coordinate system $\{\overrightarrow{e_x}, \overrightarrow{e_y}, \overrightarrow{e_z}\}$ is defined in Fig.3. The subscripts $\{i, j, k\}$ denote the spatial discretized grid points along the directions $\{x, y, z\}$, respectively. The gradient of the temperature ∇T at the center point $(x, y, z) = (i + 1/2, j - 1/2, k + 1/2)$ can be expressed by interpolation as:

$$\begin{aligned} \frac{\partial T}{\partial x}\Big|_{i+\frac{1}{2},j-\frac{1}{2},k+\frac{1}{2}} &= \frac{1}{4\Delta x} \cdot (T_{i+1,j-1,k+1} + T_{i+1,j-1,k} + T_{i+1,j,k+1} + T_{i+1,j,k} \\ &\quad - T_{i,j-1,k+1} - T_{i,j-1,k} - T_{i,j,k+1} - T_{i,j,k}) \\ \frac{\partial T}{\partial y}\Big|_{i+\frac{1}{2},j-\frac{1}{2},k+\frac{1}{2}} &= \frac{1}{4\Delta y} \cdot (T_{i+1,j,k+1} + T_{i+1,j,k} + T_{i,j,k+1} + T_{i,j,k} \\ &\quad - T_{i+1,j-1,k+1} - T_{i+1,j-1,k} - T_{i,j-1,k+1} - T_{i,j-1,k}) \\ \frac{\partial T}{\partial z}\Big|_{i+\frac{1}{2},j-\frac{1}{2},k+\frac{1}{2}} &= \frac{1}{4\Delta z} \cdot (T_{i+1,j,k+1} + T_{i+1,j-1,k+1} + T_{i,j,k+1} + T_{i,j-1,k+1} \\ &\quad - T_{i+1,j,k} - T_{i+1,j-1,k} - T_{i,j,k} - T_{i,j-1,k}) \end{aligned} \tag{4}$$

By inserting these terms into the first formula of Eq.1 and applying the diffusion tensor D, we obtain the heat flux $\overrightarrow{q}$ at the center point:

$$\overrightarrow{q}_{i+\frac{1}{2},j-\frac{1}{2},k+\frac{1}{2}} = -D_{i+\frac{1}{2},j-\frac{1}{2},k+\frac{1}{2}} \cdot \left(\frac{\partial T}{\partial x}\Big|_{i+\frac{1}{2},j-\frac{1}{2},k+\frac{1}{2}}, \frac{\partial T}{\partial y}\Big|_{i+\frac{1}{2},j-\frac{1}{2},k+\frac{1}{2}}, \frac{\partial T}{\partial z}\Big|_{i+\frac{1}{2},j-\frac{1}{2},k+\frac{1}{2}} \right)^{\mathrm{T}} \tag{5}$$

To take the divergence over the heat flux, we have the 3D formulation of the thermal conduction problem:

$$\begin{aligned} \nabla \cdot \overrightarrow{q} = & \frac{1}{4\Delta x} \cdot (q_{x,i+\frac{1}{2},j+\frac{1}{2},k+\frac{1}{2}} + q_{x,i+\frac{1}{2},j+\frac{1}{2},k-\frac{1}{2}} + q_{x,i+\frac{1}{2},j-\frac{1}{2},k+\frac{1}{2}} + q_{x,i+\frac{1}{2},j-\frac{1}{2},k-\frac{1}{2}} \\ & - q_{x,i-\frac{1}{2},j+\frac{1}{2},k+\frac{1}{2}} - q_{x,i-\frac{1}{2},j-\frac{1}{2},k+\frac{1}{2}} - q_{x,i-\frac{1}{2},j+\frac{1}{2},k-\frac{1}{2}} - q_{x,i-\frac{1}{2},j-\frac{1}{2},k-\frac{1}{2}}) + \\ & \frac{1}{4\Delta y} \cdot (q_{y,i+\frac{1}{2},j+\frac{1}{2},k+\frac{1}{2}} + q_{y,i-\frac{1}{2},j+\frac{1}{2},k+\frac{1}{2}} + q_{y,i+\frac{1}{2},j+\frac{1}{2},k-\frac{1}{2}} + q_{y,i-\frac{1}{2},j+\frac{1}{2},k-\frac{1}{2}} \\ & - q_{y,i+\frac{1}{2},j-\frac{1}{2},k+\frac{1}{2}} - q_{y,i-\frac{1}{2},j-\frac{1}{2},k+\frac{1}{2}} - q_{y,i+\frac{1}{2},j-\frac{1}{2},k-\frac{1}{2}} - q_{y,i-\frac{1}{2},j-\frac{1}{2},k-\frac{1}{2}}) + \\ & \frac{1}{4\Delta z} \cdot (q_{z,i+\frac{1}{2},j+\frac{1}{2},k+\frac{1}{2}} + q_{z,i-\frac{1}{2},j+\frac{1}{2},k+\frac{1}{2}} + q_{z,i+\frac{1}{2},j-\frac{1}{2},k+\frac{1}{2}} + q_{z,i-\frac{1}{2},j-\frac{1}{2},k+\frac{1}{2}} \\ & - q_{z,i+\frac{1}{2},j+\frac{1}{2},k-\frac{1}{2}} - q_{z,i+\frac{1}{2},j-\frac{1}{2},k-\frac{1}{2}} - q_{z,i-\frac{1}{2},j+\frac{1}{2},k-\frac{1}{2}} - q_{z,i-\frac{1}{2},j-\frac{1}{2},k-\frac{1}{2}}), \end{aligned} \tag{6}$$

where the quantities q_x, q_y and q_z are designated for the 3 components of the heat flux $\overrightarrow{q}$ along the 3 orthogonal directions $\{\overrightarrow{e_x}, \overrightarrow{e_y}, \overrightarrow{e_z}\}$.

3.2 Numerical Homogenization

As shown previously, the representative volume element (RVE) Ω is composed of two phases: the silver domain Ω_s and the air domain Ω_a. Therefore, the thermal conductivity tensor D depends on the position x inside the RVE Ω, accordingly:

$$\begin{aligned} & \Omega = \Omega_s \cup \Omega_a \\ & D(\boldsymbol{x}) = \begin{cases} D_s & \boldsymbol{x} \in \Omega_s \\ D_a & \boldsymbol{x} \in \Omega_a \end{cases} \end{aligned} \tag{7}$$

where D_s is the conductivity tensor for silver and D_a for air. The Fourier's law can be rewritten as

$$\overrightarrow{q}(\boldsymbol{x}) = -D(\boldsymbol{x}) \cdot \nabla T(\boldsymbol{x}) \tag{8}$$

The spatial averages of the local heat flux and temperature gradient are defined by:

$$< \overrightarrow{q} >= \frac{1}{|\Omega|} \int_{\Omega} \overrightarrow{q}(\boldsymbol{x}) dV \quad < \nabla T >= \frac{1}{|\Omega|} \int_{\Omega} \nabla T(\boldsymbol{x}) dV \tag{9}$$

where $|\Omega|$ is the total volume of the RVE, $\overrightarrow{q}(\boldsymbol{x})$ and $T(\boldsymbol{x})$ can be determined by applying a given temperature boundary condition; $< \overrightarrow{q} >$ and $< \nabla T >$ can be calculated by integrating the corresponding local fields over the domain Ω, then dividing it by the total volume. In the case of a two-phase problem, the integration operation is reduced to the multiplication of each $\overrightarrow{q}(x)$ and $< \nabla T(x) >$ by the volume fraction of the point at which they are located.

Consequently, the macroscopic equivalent thermal conductivity D^* is defined such that:

$$< \overrightarrow{q} >= -D^* \cdot < \nabla T > . \tag{10}$$

To numerically obtain each component of the tensor D^* in Eq.10, the RVE needs to be simulated three times by applying boundary conditions in three orthogonal directions, respectively.

3.2.1 Periodic geometry structures

The current study makes use of periodic boundary conditions for determining the equivalent thermal conductivity of the porous structures since the considered geometrical models are constructed on the basis of periodic RVEs. As described previously, periodic geometrical particle arrangements such as SC, BCC, and FCC lattices as well as their conjugated forms are selected to be investigated.

3.2.2 Periodic boundary condition and numerical algorithm

In order to study the thermal behavior of inhomogeneous materials in great detail, we need to specify the appropriate boundary conditions for the domain of interest Ω. Standard boundary conditions can be kinematically uniform (KUBC), statically uniform (SUBC), and periodic (PBC). Uniform displacement–traction (orthogonal mixed) boundary conditions (MUBC) are less known, which were introduced by Hazanov and Amieur (1995), Hazanov (1998) [28, 29]. Nemat-Nasser and Hori (1993) [30] indicated that results obtained from SUBC under-estimate the macroscopic stiffness, while KUBC over-estimates the results. Suquet (1987) [31] stated that PBC-based predictions lie between these two bounds, and Ostoja-Starzewski (2006) [32] showed that the MUBC predictions are also between the results from SUBC and KUBC. Due to the periodicity of our considered structures, periodic boundary conditions are recommended in this study for estimating the equivalent thermal conductivity of the considered unit cells with different porosities.

The definition of the periodic boundary conditions for elasticity problems can be expressed as the following equation:

$$\boldsymbol{u}^{+}(\boldsymbol{x}) - \boldsymbol{u}^{-}(\boldsymbol{x}) = \boldsymbol{\varepsilon}^{0}\Delta x, \quad \forall \boldsymbol{x} \in \partial\Omega \tag{11}$$

where $\boldsymbol{u}^{+}$ and $\boldsymbol{u}^{-}$ denote the displacement field on a pair of parallel boundary surface, Δx denotes the constant distance between parallel planes and $\boldsymbol{\varepsilon}^{0}$ is a given macroscopic strain.

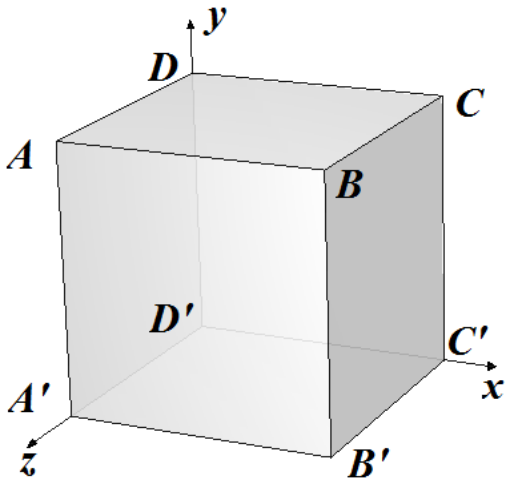

Figure 4: RVE with periodic boundary conditions

The PBC for temperature field T is similarly created. By substituting the u to the temperature T, and the term $\boldsymbol{\varepsilon}^{0}\Delta x$ to the temperature variation ΔT in Eq.11, we obtain:

$$\boldsymbol{T}^{+}(\boldsymbol{x}) - \boldsymbol{T}^{-}(\boldsymbol{x}) = \Delta T, \quad \forall \boldsymbol{x} \in \partial\Omega \tag{12}$$

More specially, the equations applied in a lattice (see Fig.4) to predict the equivalent thermal conductivity are shown below:

· Face-BCC′B′ and Face-ADD′A′:

$$T_{Face-BCC'B'} - T_{Face-ADD'A'} = \Delta T_x \tag{13}$$

· Face-ADCB and Face-A′D′C′B′:

$$T_{Face-ADCB} - T_{Face-A'D'C'B'} = \Delta T_y \tag{14}$$

· Face-ABB′A′ and Face-DCC′D′:

$$T_{Face-ABB'A'} - T_{Face-DCC'D'} = \Delta T_z \tag{15}$$

· Edge-AA′, Edge-BB′, Edge-CC′ and Edge-DD′:

$$\begin{aligned} T_{Edge-AA'} - T_{Edge-DD'} &= \Delta T_z \\ T_{Edge-CC'} - T_{Edge-DD'} &= \Delta T_x \\ T_{Edge-BB'} - T_{Edge-CC'} &= \Delta T_z \end{aligned} \tag{16}$$

· Edge-AB, Edge-DC, Edge-D′C′ and Edge-A′B′:

$$\begin{aligned} T_{Edge-AB} - T_{Edge-A'B'} &= \Delta T_y \\ T_{Edge-AB} - T_{Edge-DC} &= \Delta T_z \\ T_{Edge-DC} - T_{Edge-D'C'} &= \Delta T_y \end{aligned} \tag{17}$$

· Edge-BC, Edge-B′C′, Edge-A′D′ and Edge-AD:

$$\begin{aligned} T_{Edge-BC} - T_{Edge-AD} &= \Delta T_x \\ T_{Edge-BC} - T_{Edge-B'C'} &= \Delta T_y \\ T_{Edge-B'C'} - T_{Edge-A'D'} &= \Delta T_x \end{aligned} \tag{18}$$

· Vertice-A, Vertice-B, Vertice-C and Vertice-D:

$$\begin{aligned} T_{Vertice-A} - T_{Vertice-D} &= \Delta T_z \\ T_{Vertice-C} - T_{Vertice-D} &= \Delta T_x \\ T_{Vertice-B} - T_{Vertice-C} &= \Delta T_z \end{aligned} \tag{19}$$

· Vertice-A′, Vertice-B′, Vertice-C′ and Vertice-D′:

$$\begin{aligned} T_{Vertice-A'} - T_{Vertice-D'} &= \Delta T_z \\ T_{Vertice-C'} - T_{Vertice-D'} &= \Delta T_x \\ T_{Vertice-B'} - T_{Vertice-C'} &= \Delta T_z \end{aligned} \tag{20}$$

· Vertice-B and Vertice-B′:

$$T_{Vertice-B} - T_{Vertice-B'} = \Delta T_y \tag{21}$$

where ΔT_x, ΔT_y and ΔT_z are the difference of temperature between Face-BCC′B′ and Face-ADD′A′, between Face-ADCB and Face-A′D′C′B′ and between Face-ABB′A′ and Face-DCC′D′, respectively. In order to calculate the components (D_{ij}) of the composite's equivalent thermal conductivity tensor, the RVE must be numerically simulated three times using suitable magnitudes ΔT_x, ΔT_y and ΔT_z .

In anisotropic case, the thermal conductivity tensor D^* has 9 components. To calculate the components D^*_{11}, D^*_{21}, D^*_{31}, the following values could be applied:

$$\Delta T_x \neq 0, \quad \Delta T_y = 0, \quad \text{and} \quad \Delta T_z = 0 \tag{22}$$

To calculate the components D^*_{12}, D^*_{22}, D^*_{23}:

$$\Delta T_x = 0, \quad \Delta T_y \neq 0, \quad \text{and} \quad \Delta T_z = 0 \tag{23}$$

To calculate the components D^*_{13}, D^*_{23}, D^*_{33}:

$$\Delta T_x = 0, \quad \Delta T_y = 0, \quad \text{and} \quad \Delta T_z \neq 0 \tag{24}$$

In isotropic case, the tensor D^* is diagonal and can be reduced as $D^* = k^* I$, where the k^* is the scalar thermal conductivity. Our research is concentrated on isotropic situations as the studied geometric configurations are macroscopically isotropic.

4 Results and comparisons

In this section, we will display the results obtained by our home-made finite difference (FD) codes. For the sake of code verification, the finite element (FE) simulation results based on the Comsol Multiphysics program are used as benchmarks. First, we take the BCC structure as an example to analyze the mesh convergence. Then, the simulated local fields (such as the temperature field and the heat flux field) by FD are compared with that by FE. Finally, the equivalent thermal conductivity is calculated as a function of porosity and also compared with the theoretical formula.

4.1 Convergence analysis and computational time

The convergence analysis is applied to a case of the unit BCC structure, where the sphere radii are all equal to 0.46, thus resulting in a volume fraction of 79.89%. The boundary conditions we used are described in Eq.22 such that $\Delta T_x = 1$, $\Delta T_y = 0$, and $\Delta T_z = 0$. We fix the temperature of one vertex on the left side to 19°C so that the right side is 20°C (room temperature). The thermal conductivity of silver is 429 W· m^{-1}·K^{-1} and that of air is 0.0257 W· m^{-1}·K^{-1}. To study the convergence of thermal conductivity, different refinements of mesh-grid are used, i.e. from 10 thousand to 2 million elements. The results are shown in Table 1 and in Fig.5a.

Table 1: Convergence results of different mesh levels by FED and FEM.

Number of voxel cells by FDM	15625	91125	274625	614125	1953125
Equivalent thermal conductivity	233.09	232.04	229.26	226.23	224.79
Number of finite elements	17677	36961	132968	446553	2348718
Equivalent thermal conductivity	227.54	226.10	224.38	223.86	223.35

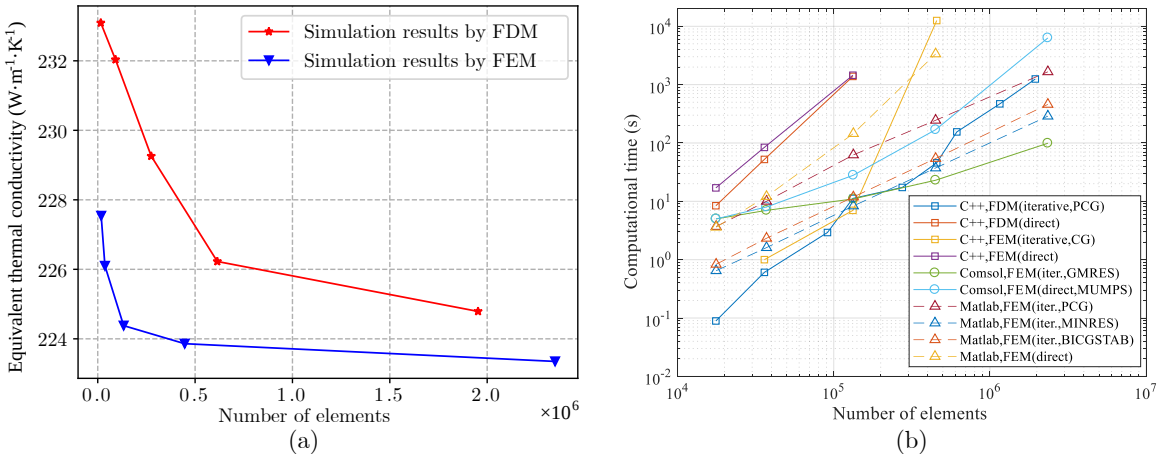

Figure 5: Illustration of (a) convergence and (b) computational time

According to Fig.5a, we find that firstly, the equivalent thermal conductivity exhibits some fluctuations but they are reasonable. These small fluctuations can be explained by the nature of voxel meshing which results in slight variations of the volume fraction of silver when the mesh density is increased. Secondly, the convergence rate of the finite difference method is very close to that of FEM, which shows the stability and robustness of the FD algorithm. Finally, when we compare the equivalent thermal conductivity obtained for a number of elements greater than 500 thousand elements, the results remain nearly unchanged (226 W· m^{-1}·K^{-1} by FDM, 224 W· m^{-1}·K^{-1} by FEM) and the error between the two methods is less than 1%.

Furthermore, we have compared the computational time from different algorithms with different platforms when solving the system of linear equations (see Fig.5b). Our developed FD codes (by C++ routine) is based on the library "EIGEN". Direct and iterative solvers are tested for comparison. Algorithms by Comsol and Matlab are also illustrated as benchmarks. Three iterative solvers (PCG, MINRES, BICGSTAB) are used in Matlab. Default direct solvers are used when not indicated in the legend. It can be seen from the figure that: (i) the computational time depends considerably on the algorithms and solvers; (ii) the iterative methods are generally faster than the direct methods; (iii) the developed FD codes with iterative algorithm (the solid line with blue squared marker) manifest a pertinent and preferable computational time when compared with other curves.

Thereafter, we will use the FD system that we developed to calculate and compare the temperature field and the heat flow field for different geometrical models at different porosities.

4.2 Simulation results of local fields

To proceed with the comparison of local fields, several geometrical models are selected as examples in this section. The first one is the SC model with the volume fraction of silver equal to 67.18%, which is shown in Fig.6 (corresponding to a sphere radius equal to 0.55). The overall temperature field (see Fig.6a for FDM, Fig.6b for FEM) and heat flux field (see Fig.6c for FDM, Fig.6d for FEM) as well as their middle cross sections (see Fig.6e-h) are displayed. The unit structure is divided into $45 \times 45 \times 45 = 91125$ cubic voxel cells by FDM, while it is divided into 31460 tetrahedral finite elements by FEM. We can see from the figure that the distributions of the temperature and the heat flux fields by the two methods are comparable and consistent, which demonstrates again the validity of the FD system we developed in this study.

The results for the SC conjugated model are shown in Fig.7. The fraction of silver is 32.82%. The numbers of voxel cells and that of finite elements are the same as in the non-conjugated model. It can be seen that the temperature and the heat flux fields in this situation by the two methods are also matched and coordinated, which shows the effectiveness of the FD algorithm in the conjugated model.

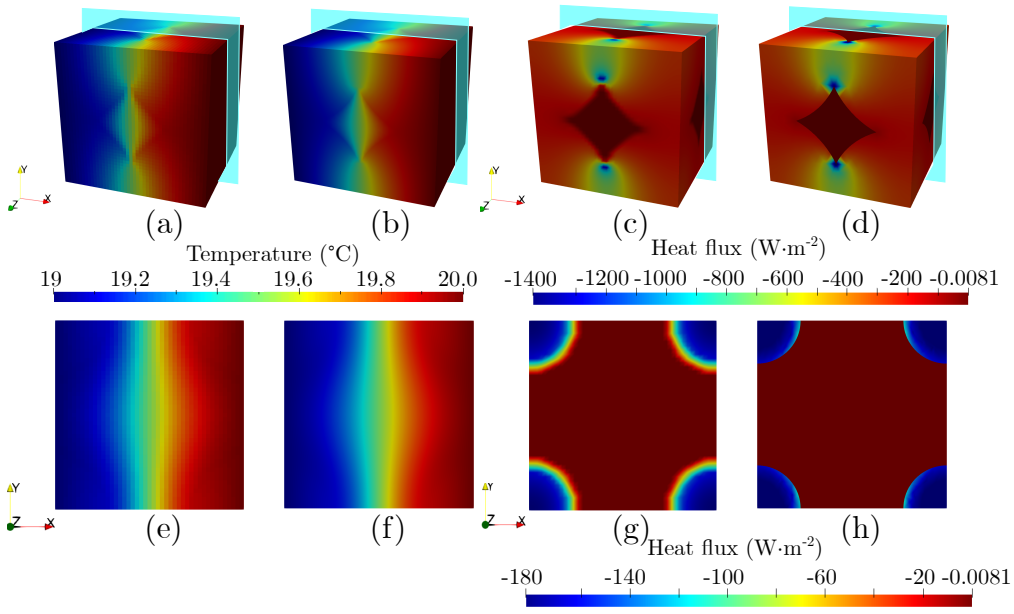

Figure 6: SC model with the volume fraction of silver equal to 67.18%: (a) temperature field by FDM, (b) temperature field by FEM, (c) heat flux field by FDM, (d) heat flux field by FEM, (e) temperature field in cross section xOy by FDM, (f) temperature field in cross section xOy by FEM, (g) heat flux field in cross section xOy by FDM, (h) heat flux field in cross section xOy by FEM.

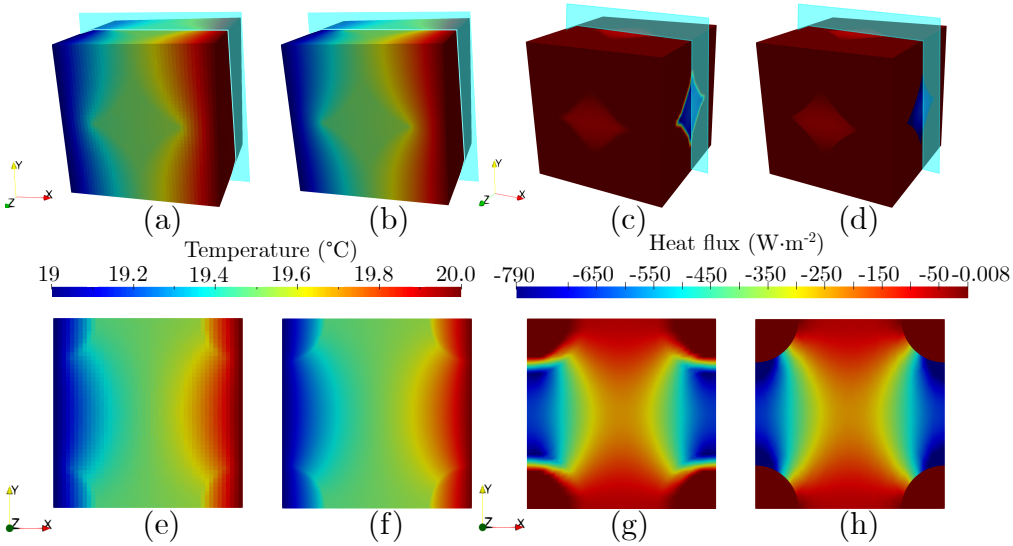

Figure 7: SC conjugated model with the volume fraction of silver equal to 32.82%: (a) temperature field by FDM, (b) temperature field by FEM, (c) heat flux field by FDM, (d) heat flux field by FEM, (e) temperature field in cross section xOy by FDM, (f) temperature field in cross section xOy by FEM, (g) heat flux field in cross section xOy by FDM, (h) heat flux field in cross section xOy by FEM.

The second model is the BCC structure with the volume fraction of silver equal to 79.89%, which is shown in Fig.8 (corresponding to a sphere radius equal to 0.46). The structure contains 91125 cubic voxel cells by FDM, and 36961 tetrahedral finite elements by FEM. Meanwhile, Fig.9 displays the BCC conjugated model with the fraction of silver being 20.11%. Both the temperature field and the heat flux field exhibit good agreement in terms of trends and values.

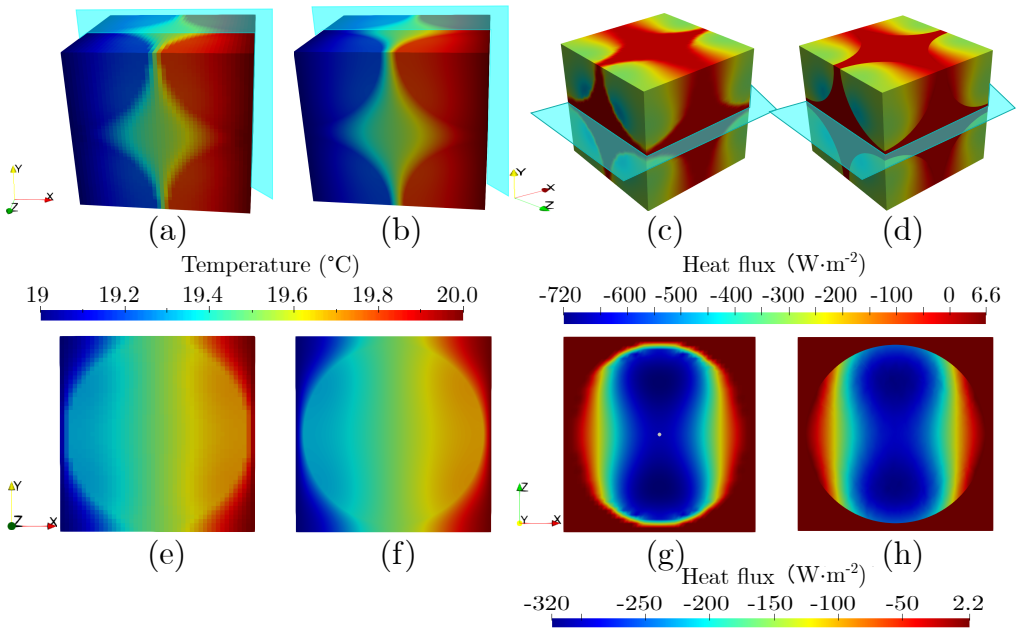

Figure 8: BCC model with the volume fraction of silver equal to 79.89%: (a) temperature field by FDM, (b) temperature field by FEM, (c) heat flux field by FDM, (d) heat flux field by FEM, (e) temperature field in cross section xOy by FDM, (f) temperature field in cross section xOy by FEM, (g) heat flux field in cross section xOy by FDM, (h) heat flux field in cross section xOy by FEM.

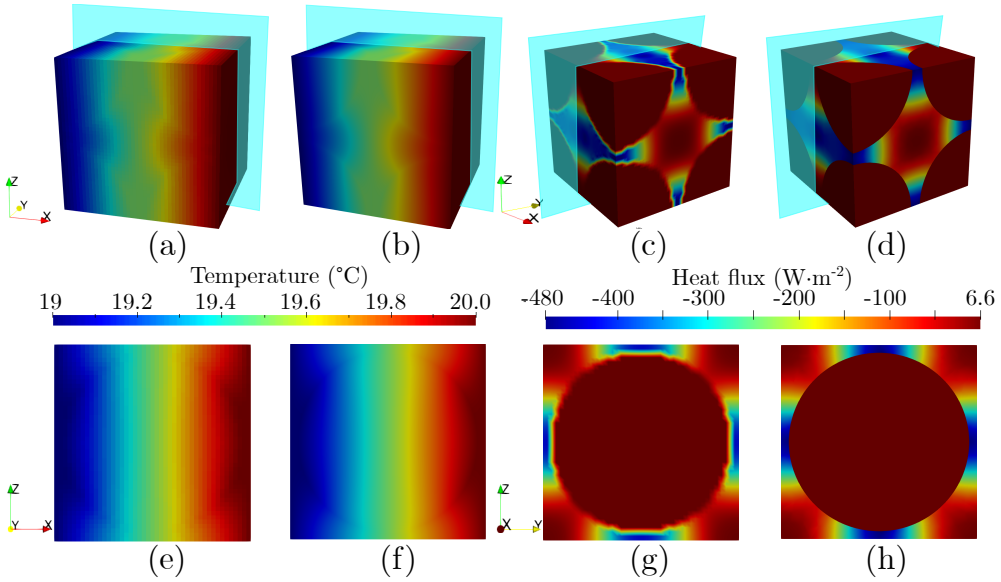

Figure 9: BCC conjugated model with the volume fraction of silver equal to 20.11%: (a) temperature field by FDM, (b) temperature field by FEM, (c) heat flux field by FDM, (d) heat flux field by FEM, (e) temperature field in cross section xOy by FDM, (f) temperature field in cross section xOy by FEM, (g) heat flux field in cross section xOz by FDM, (h) heat flux field in cross section xOz by FEM.

The third geometrical model is the FCC structure with the volume fraction of silver equal to 88.07%, which corresponds to a sphere radius equal to 0.38. The structure contains 91125 cubic voxel cells by FDM, and 35340 tetrahedral finite elements by FEM. The results of local fields are shown in Fig.10, and the FCC conjugated model with the fraction of silver equal to 20.11% is analyzed in Fig.11. One can find similar trends with the previous geometries, thus similar conclusions can be drawn. To sum up, the developed FDM algorithm can treat a series of situations and has some advantages such as: (i) it uses simple rule of voxel meshing to reduce the computational time; (ii) it has a good anti-sawtooth ability and can get rid of the constraint of the interface between the silver and the air; (iii) FDM can obtain comparable results as the finite element method.

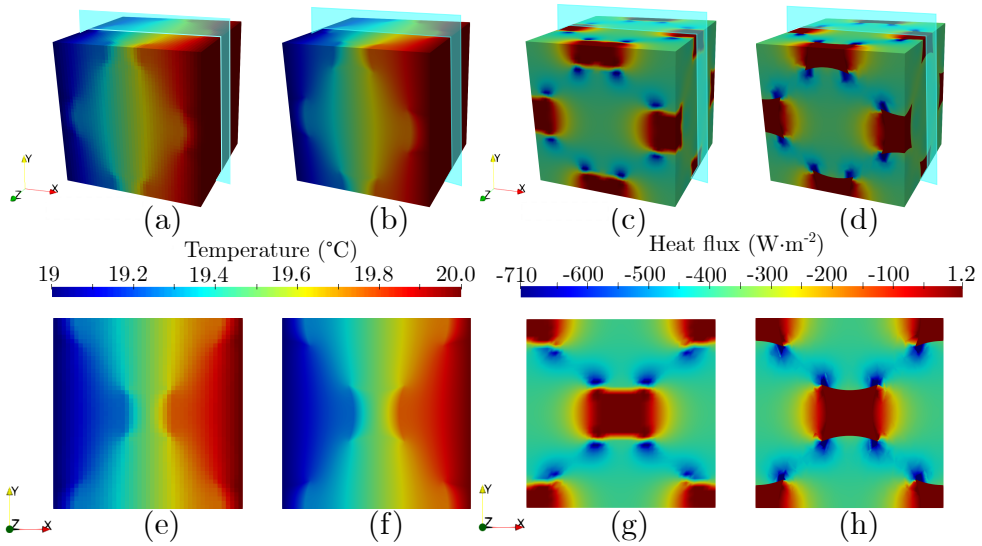

Figure 10: FCC model with the volume fraction of silver equal to 88.07%: (a) temperature field by FDM, (b) temperature field by FEM, (c) heat flux field by FDM, (d) heat flux field by FEM, (e) temperature field in cross section xOy by FDM, (f) temperature field in cross section xOy by FEM, (g) heat flux field in cross section xOy by FDM, (h) heat flux field in cross section xOy by FEM.

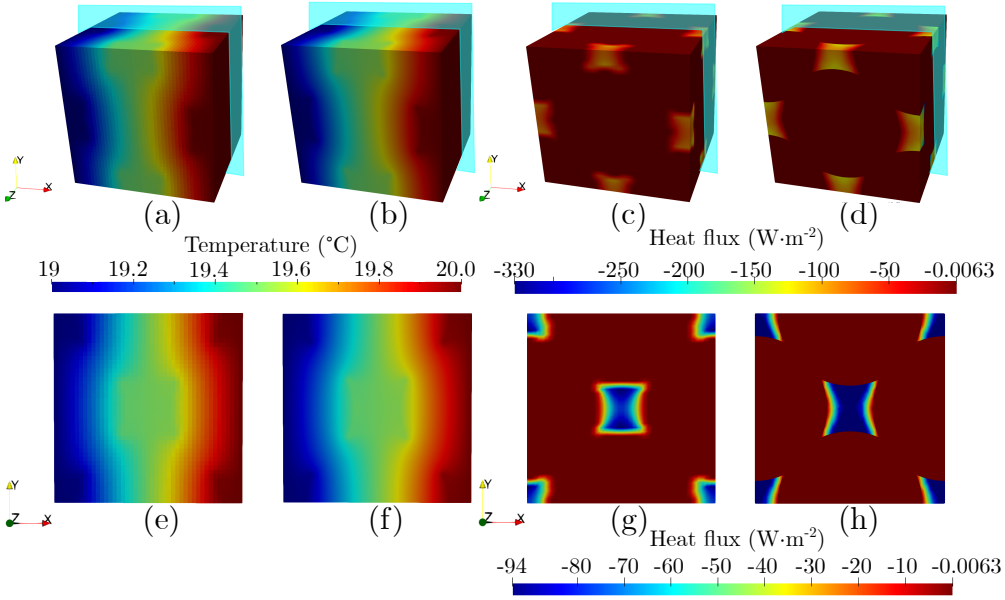

Figure 11: FCC conjugated model with the volume fraction of silver equal to 11.93%: (a) temperature field by FDM, (b) temperature field by FEM, (c) heat flux field by FDM, (d) heat flux field by FEM, (e) temperature field in cross section xOy by FDM, (f) temperature field in cross section xOy by FEM, (g) heat flux field in cross section xOy by FDM, (h) heat flux field in cross section xOy by FEM.

4.3 Evolution of the equivalent thermal conductivity

In this section, we calculate the equivalent thermal conductivity of the aforementioned models by using Eq.10 for various volume fraction of silver. To make the volume fraction of silver vary in a given unit cell (SC, BCC or FCC), the positions of the corresponding silver particles are kept unchanged while their radii are uniformly increased to reduce the voids. The results of the simulations are shown in Fig.12. We draw the following

observations:

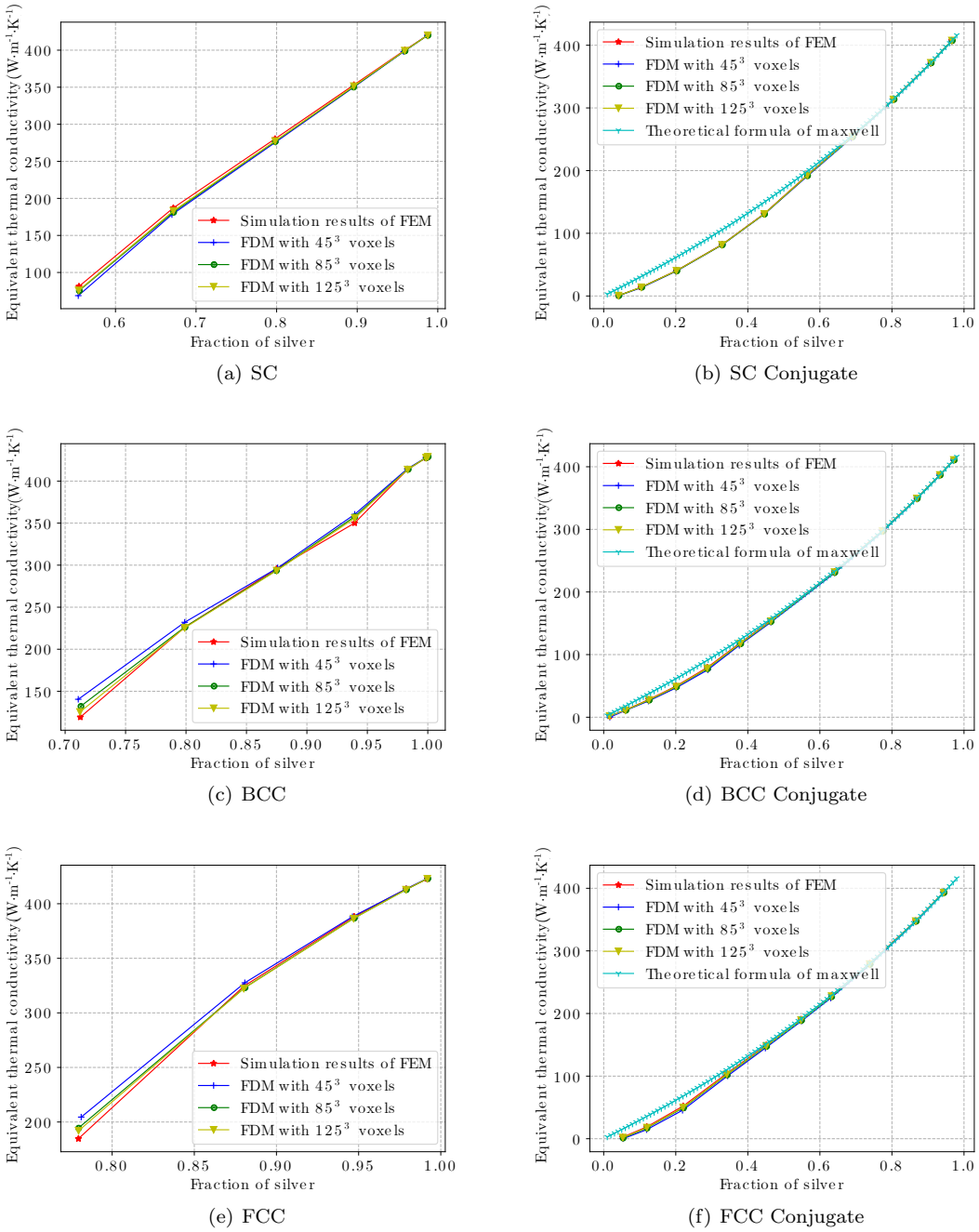

(a) SC (b) SC Conjugate

(c) BCC (d) BCC Conjugate

(e) FCC (f) FCC Conjugate

Figure 12: Evolution of the equivalent thermal conductivity as a function of the volume fraction for the various models. The star symbols represent the values obtained by FEM. The cross symbols, the circle markers, the triangle-down markers correspond to the values of FDM with $45 \times 45 \times 45$, $85 \times 85 \times 85$ and $125 \times 125 \times 125$ voxels, respectively. The tree markers designate the values calculated by theoretical formula of Maxwell.

(1) The equivalent thermal conductivities of SC, BCC, FCC, and their conjugated models increase with the increase of the silver fraction. This is consistent with the fact that the conductivity of silver (429 W$\cdot$ m$^{-1}\cdot$K^{-1}) is larger than the air's one (0.0257 W$\cdot$ m$^{-1}\cdot$K^{-1}).

(2) From Fig.12a,c,e, one can find that as the silver volume fraction increases, a better agreement between the FDM and the FEM results is found. The largest difference between the two methods in the three models occurs for the lowest values of the silver volume fraction when the silver particles are just contacting each

other in the respective unit cells (i.e. the radius of spherical silvers for SC model is 0.5, for BCC model is $\sqrt{3}/4 \approx 0.433$, for FCC model is $\sqrt{2}/4 \approx 0.354$; and the corresponding volume fraction of silver for SC model is 0.555, for BCC model is 0.713, for FCC model is 0.779). This is caused by the inherent property of the voxel meshing which has poor capabilities for approximating curved surfaces like those of the spherical silver particles. Voxel meshing produces sawtooth shaped surfaces when mesh density is small. By increasing the mesh density, the values of FDM gradually tend to those of FEM. It is to say that the FDM is more sensitive to lower volume fractions of silver, especially when the spheres are merely contacting.

(3) In contrast, from Fig.12b,d,f, one could not find the similar sensitivities. It is because for the conjugated models, the silvers regions are connected in a different way. The conjugated connections ensure that the silver phase forms always a contiguous part. Consequently, the volume fraction of silver can take values in a wider range (i.e. from 0 to 1). We can see that the results obtained from FDM for different mesh densities and from FEM are superimposed very well at both low and high fraction values. We also introduce Maxwell's analytic formula [4]:

$$\frac{D_{eq}}{D_m} = 1 + \frac{3\phi}{(\frac{D_f + 2D_m}{D_f - D_m}) - \phi} \tag{25}$$

where D_m represents the thermal conductivity of matrix, D_f the thermal conductivity of fillers, D_{eq} the equivalent conductivity of the whole structure, and ϕ is the volume fraction of fillers. This formula is valid only in the case of low ϕ according to Pietrak et al. [6] (under about 25%), which corresponds to the situation when the volume fraction of silver is above 75%. When comparing all the three results, it turns out that the FDM and the FEM curves can fit well with the Maxwell's formula not only in the expected fraction, but also between 50% and 75%. This proves the accuracy and effectiveness of the finite difference algorithm, even in a sparse mesh density of 45^3.

Fig.13 compares the equivalent thermal conductivity of SC, BCC and FCC models. One can find that the value of this property for the SC structure is larger than the ones for the BCC/FCC structures for an identical fraction of silver (or porosity). It indicates that changing the inner organization pattern of a structure can significantly impact its thermal property.

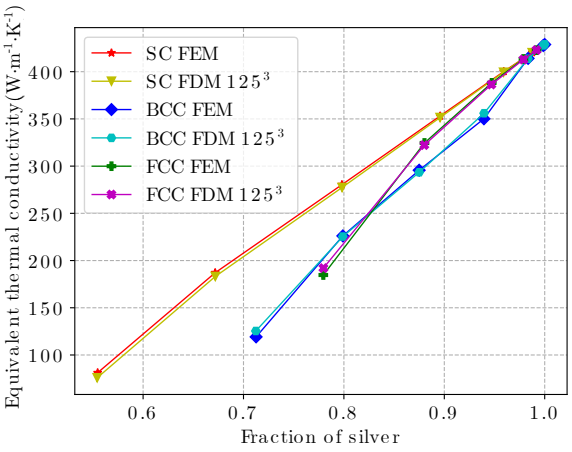

Figure 13: Comparison of the equivalent thermal conductivity between the SC, BCC and FCC models.

Fig.14 compares the equivalent thermal conductivities of the non-conjugated models with those of the corresponding conjugated models. It can be found that the results for the conjugated structures are larger than the ones for the non-conjugated structures for the three models, when making the comparison at the same porosity. This confirms that the conjugated structures are more conductive. By altering the topology or morphology of a structure, the thermal property can thus be changed greatly.

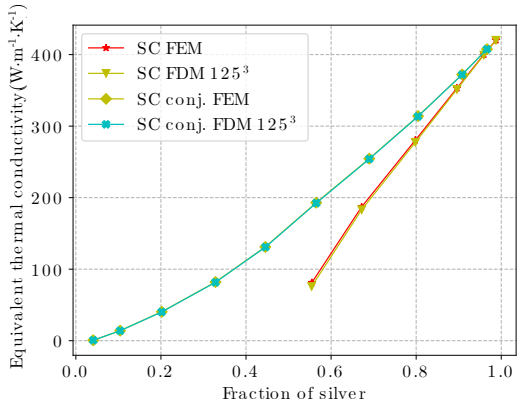

(a) SC and SC conjugated models

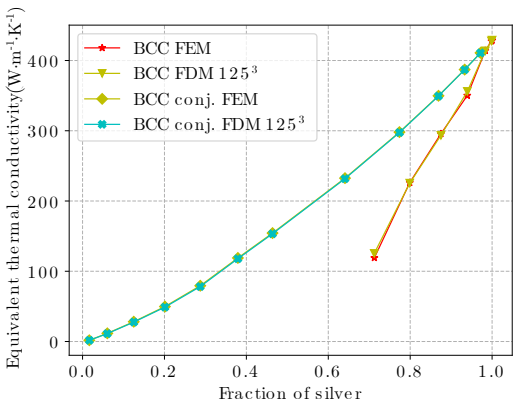

(b) BCC and BCC conjugated models

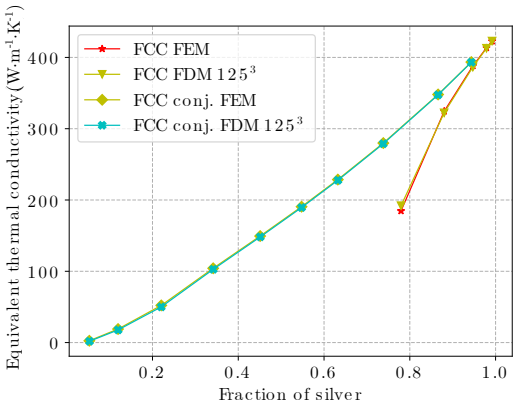

(c) FCC and FCC conjugated models

Figure 14: Comparison of equivalent thermal conductivity between the non-conjugated and the conjugated models.

5 Stochastic granular models

To further test the usability of the developed FD algorithm in other situations, we additionally consider a kind of stochastic models. Fig.15 illustrates the geometrical models of the stochastic structure. The structures are set to unit size and composed of two phases: silver and air. In order to make the spherical silver particles connect with each other to form a continuous entirety, an overlap is proposed herein (for example, this can mimic the neck formation between silver particles after the sintering process). The generation method of these spheres is discussed in [27, 33]. Here, 56 spheres are generated, and their radii obey a normal distribution. In Figs.15, three cases are considered: Case 1 is a stochastic model with minimal overlap between particles, having an average particle radius of 0.139 and a standard deviation of 0.026 (silver fraction = 0.663); Case 2 is a stochastic model with a larger overlap, having an average particle radius of 0.146 and a standard deviation of 0.028 (silver fraction = 0.734); and Case 3 is the conjugated structure of Case 2 with an average particle radius of 0.059 and a standard deviation of 0.011, i.e., keeping the silver fraction constant (silver fraction = 0.734) and replacing the silver phase with air and the air phase with silver (this can mimic the situation of air bubbles in solids). To ensure the periodicity of these models, spheres that go out from one surface will be enforced to re-enter from the opposite surface. The simulation results of the equivalent thermal conductivity are shown in Table 2.

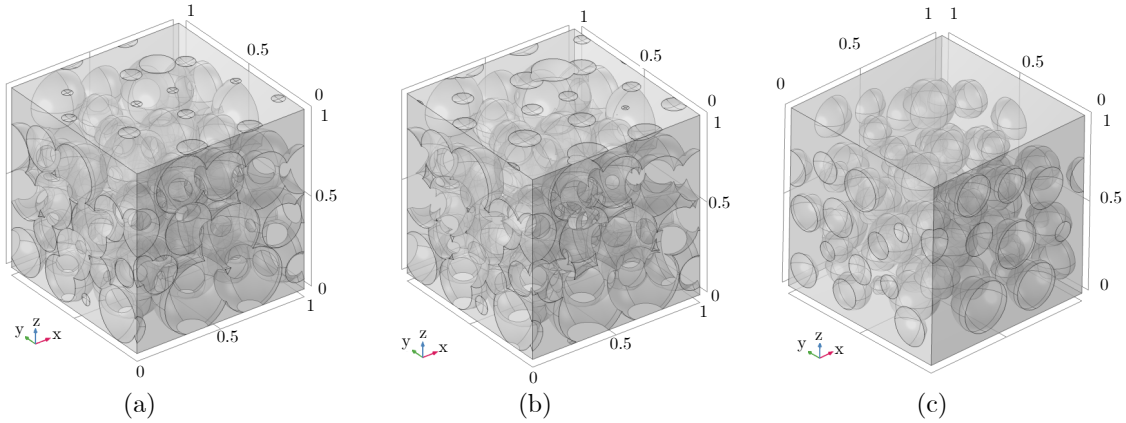

Figure 15: Geometrical illustration of three random models. (a) case 1: volume fraction of silver = 66.3%, (b) case 2: volume fraction of silver = 73.4% , (c) case 3: conjugated structure with volume fraction of silver = 73.4% (i.e. the silver is for the matrix, and the air is for the sphere inclusion).

Table 2: Comparison of the equivalent thermal conductivity for random models with FDM and FEM.

	Mean value μ of sphere radius	Standard deviation σ of sphere radius	Silver fraction	D_{xx} by FDM	D_{xx} by FEM	Relative error
Case 1 (Silver spheres)	0.139	0.026	0.663	188.8	178.3	5.87%
Case 2 (Silver spheres)	0.146	0.028	0.734	248.9	239.8	3.66%
Case 3 (Air spheres)	0.059	0.011	0.734	278.9	278.3	0.216%

By comparing Case 1 and Case 2, we find that the equivalent thermal conductivity obtained by the two methods are very similar, and the finite difference method is closer to the finite element method as the overlap portion increases. This result also verifies our conclusion in the previous section that the voxelized mesh does not simulate the interfaces well when the material with a larger thermal conductivity has a narrow connection area. By comparing the equivalent thermal conductivity in Case 2 and Case 3, it can be found that the FD simulation of the conjugated structure is better than that of the normal structure when the silver fraction remains the same. The relative errors of the three cases are all below 6%.

Fig. 16 shows the random model with the fraction of silver equal to 73.4% (corresponding to an average radius of 0.146 and a standard deviation of 0.028). The structure contains 614125 cubic voxel cells by FDM, and 473920 tetrahedral finite elements by FEM. By comparing the temperature fields (see Fig.16a,b,e,f), we find that the distributions obtained by the two methods are quite consistent. If comparing the distribution of the heat flux field (see Fig.16c,d,g,h), it is shown that the overall trend is the same, but in some junctions between different silver spheres, the finite element method is slightly better than the finite difference method, which is caused by the voxelized mesh, as the silver sphere connections inside the random system are more complex and require a more dense mesh to approximate finely the curved interfaces at these locations.

Fig. 17 shows the conjugated random model with the fraction of silver equal to 73.4% (corresponding to an average radius of 0.059 and a standard deviation of 0.011). The structure contains 614125 cubic voxel cells by FDM, and 94396 tetrahedral finite elements by FEM. From the figures we can see that both the distributions of the temperature and of the heat flux fields by the two methods are almost identical.

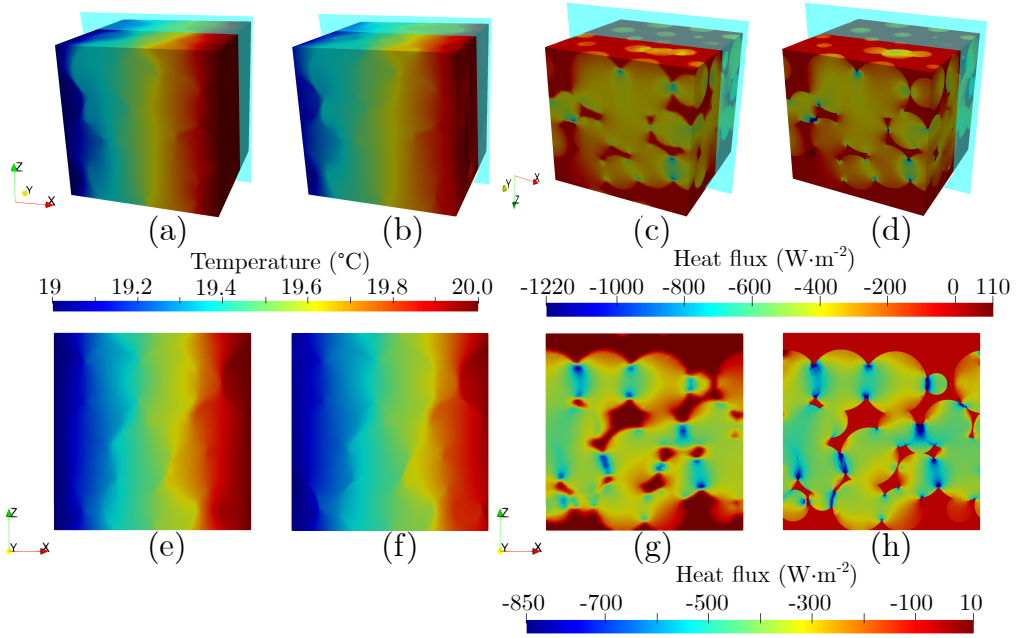

Figure 16: Stochastic model with the volume fraction of silver equal to 73.4%: (a) temperature field by FDM, (b) temperature field by FEM, (c) heat flux field by FDM, (d) heat flux field by FEM, (e) temperature field in cross section xOz by FDM, (f) temperature field in cross section xOz by FEM, (g) heat flux field in cross section yOz by FDM, (h) heat flux field in cross section yOz by FEM.

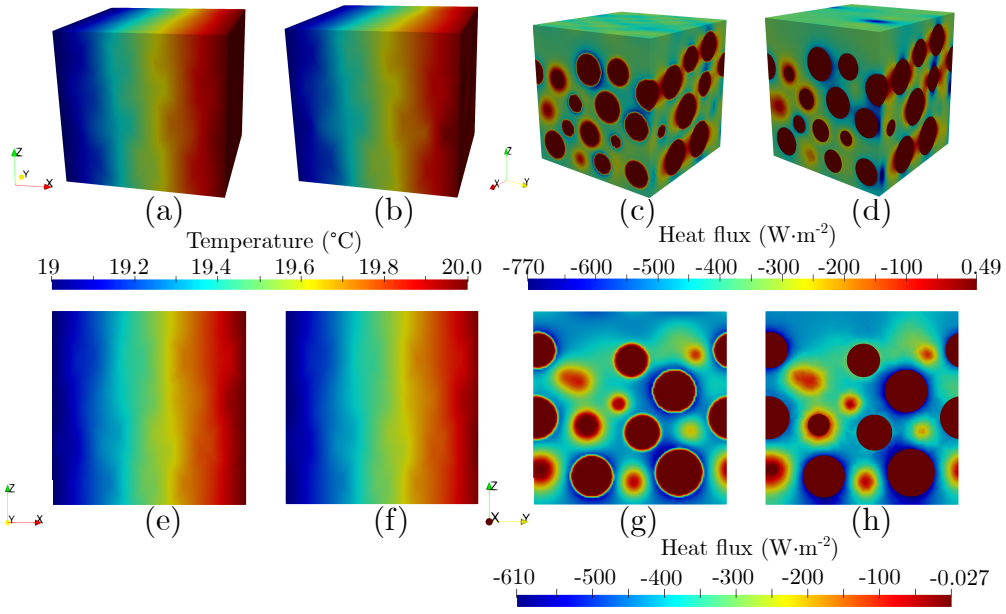

Figure 17: Stochastic conjugated model with the volume fraction of silver equal to 73.4%: (a) temperature field by FDM, (b) temperature field by FEM, (c) heat flux field by FDM, (d) heat flux field by FEM, (e) temperature field in cross section xOz by FDM, (f) temperature field in cross section xOz by FEM, (g) heat flux field in cross section yOz by FDM, (h) heat flux field in cross section yOz by FEM.

6 Conclusions and perspectives

In this paper, we developed a voxel-based finite difference method to investigate the equivalent thermal conductivity of various composite materials or structures. The structures are spherical filler models and composed of two phases: silver and air. Three typical geometries (SC, BCC, FCC models) as well as stochastic models are analyzed. Comparisons are carried out with the finite element method and the theoretical formula of Maxwell. The following conclusions can be summarized.

First, our proposed algorithm yielded comparable results with the FEM, whether when handling the classical SC, BCC, FCC models or complex stochastic models. Second, the developed FD algorithm is less sensitive to the density of mesh and has a good anti-sawtooth ability. Finally, with the natural advantage of FDM in parallel computing, the proposed method is scalable in terms of computational efficiency.

For perspectives regarding other approaches to calculate thermal properties, atomistic or molecular simulation method might also be considered. However, difficulties or limitations persist in the current circumstance. As for the atomistic simulation, a DFT-based ab-initio calculation could deal with this scenario; but it is challenging to compute silver clusters of such size since the spherical particle mentioned in the study is of micrometer scale. It means that a single particle may contain billions of atoms and the state-of-the-art technology still lacks computational power.

As for the method of molecular dynamics (MD) which may carry a larger model, the dominant influencing factor in thermal conduction of a metal is the electron, rather than the phonon. Ab-initio MD based two-temperature model may solve the coupling problem of electrons and phonons, but it is normally for bulk materials instead of porous ones, as the electron grid is difficult to be coupled into the interfaces between pores and phonon lattices. Hence, new coupling algorithms are expected to be developed.

Furthermore, mounting experiments to measure the thermal conductivity is a whole subject that is being studied and implemented, in particular with AFM microscope equipped with tips meant for electric measurements. We leave this extension for future work.

Declaration of Competing Interest

The authors declare that they have no known competing financial interests or personal relationships that could have appeared to influence the work reported in this paper.

Data Availability

The data that support the findings of this study are available upon reasonable request.

Acknowledgments

This work is supported by the National Natural Science Foundation of China (Grant No. 52205269). The authors also appreciate the discussions with Dr. Weizhi LUO from University of Gustave Eiffel during the revision of the article.

References

[1] W. Voigt. Ueber die beziehung zwischen den beiden elasticitätsconstanten isotroper körper. *Annalen der Physik*, 274(12):573–587, 1889.

[2] A. Reuss. Berechnung der fließgrenze von mischkristallen auf grund der plastizitätsbedingung für einkristalle . *ZAMM - Journal of Applied Mathematics and Mechanics / Zeitschrift für Angewandte Mathematik und Mechanik*, 9(1):49–58, 1929.

[3] Z. Hashin and S. Shtrikman. A variational approach to the theory of the effective magnetic permeability of multiphase materials. *Journal of Applied Physics*, 33(10):3125–3131, 1962.

[4] J. C. Maxwell. A treatise on electricity and magnetism. 1873.

[5] A. Eucken. Die wärmeleitfähigkeit keramischer feuerfester stoffe : ihre berechnung aus der wärmeleitfähigkeit der bestandteile. 1932.

[6] K. Pietrak and T. Wiśniewski. A review of models for effective thermal conductivity of composite materials. *Journal of Power Technologies*, 95(1):14–24, 2014.

[7] A. El Moumen, T. Kanit, A. Imad, and H. El Minor. Computational thermal conductivity in porous materials using homogenization techniques: Numerical and statistical approaches. *Computational Materials Science*, 97:148–158, 2015.

[8] J. P. M. Florez, M. B. H. Mantelli, and G. G. V. Nuernberg. Effective thermal conductivity of sintered porous media: Model and experimental validation. *International Journal of Heat and Mass Transfer*, 66:868–878, 2013.

[9] L. Signor, P. Kumar, B. Tressou, C. Nadot-Martin, J. Miranda-Ordonez, J. Carr, K. Joulain, and X. Milhet. Evolution of the Thermal Conductivity of Sintered Silver Joints with their Porosity Predicted by the Finite Element Analysis of Real 3D Microstructures. *Journal of Electronic Materials*, 47(7):4170–4176, July 2018.

[10] F. Qin, Y. Hu, Y. Dai, T. An, P. Chen, Y. Gong, and H. Yu. Crack Effect on the Equivalent Thermal Conductivity of Porously Sintered Silver. *Journal of Electronic Materials*, 49(10):5994–6008, July 2020.

[11] F. Qin, Y. Hu, Y. Dai, T. An, and P. Chen. Evaluation of thermal conductivity for sintered silver considering aging effect with microstructure based model. *Microelectronics Reliability*, 108:113633, 2020.

[12] A. Abdulle and W. E. Finite difference heterogeneous multi-scale method for homogenization problems. *Journal of Computational Physics*, 191(1):18–39, 2003.

[13] F. Chen and L. Ren. Application of the finite difference heterogeneous multiscale method to the richards' equation. *Water Resources Research*, 44(7), 2008.

[14] F. Chen and L. Ren. New scheme of finite difference heterogeneous multiscale method to solve saturated flow in porous media. *Abstract and Applied Analysis*, 2014:1–19, 03 2014.

[15] M. Shashkov and S. Steinberg. Support-operator finite-difference algorithms for general elliptic problems. *Journal of Computational Physics*, 118(1):131–151, 1995.

[16] M. Shashkov and S. Steinberg. Solving diffusion equations with rough coefficients in rough grids. *Journal of Computational Physics*, 129(2):383–405, 1996.

[17] J. M. Hyman and M. Shashkov. Approximation of boundary conditions for mimetic finite-difference methods. *Computers & Mathematics with Applications*, 36(5):79–99, 1998.

[18] J. E. Morel, M. L. Hall, and M. J. Shashkov. A local support-operators diffusion discretization scheme for hexahedral meshes. *Journal of Computational Physics*, 170(1):338–372, 2001.

[19] J. E. Morel, R. M. Roberts, and M. J. Shashkov. A local support-operators diffusion discretization scheme for quadrilateral r-z meshes. *Journal of Computational Physics*, 144(1):17–51, 1998.

[20] J. E. Morel, J. E. Dendy, M. L. Hall, and S. W. White. A cell-centered lagrangian-mesh diffusion differencing scheme. *Journal of Computational Physics*, 103(2):286–299, 1992.

[21] S. Günter, Q. Yu, J. Krüger, and K. Lackner. Modelling of heat transport in magnetised plasmas using non-aligned coordinates. *Journal of Computational Physics*, 209(1):354–370, 2005.

[22] B. van Es, B. Koren, and H. J. de Blank. Finite-difference schemes for anisotropic diffusion. *Journal of Computational Physics*, 272:526–549, 2014.

[23] J. A. Soler, F. Schwander, G. Giorgiani, J. Liandrat, P. Tamain, and E. Serre. A new conservative finite-difference scheme for anisotropic elliptic problems in bounded domain. *Journal of Computational Physics*, 405:109093, 2020.

[24] M. Hölzl, S. Günter, Q. Yu, and K. Lackner. Numerical modeling of diffusive heat transport across magnetic islands and highly stochastic layers. *Physics of Plasmas*, 14(5), 2007. cited By 19.

[25] S. Günter, K. Lackner, and C. Tichmann. Finite element and higher order difference formulations for modelling heat transport in magnetised plasmas. *Journal of Computational Physics*, 226(2):2306–2316, 2007. cited By 33.

[26] G. Giorgiani, H. Bufferand, F. Schwander, E. Serre, and P. Tamain. A high-order non field-aligned approach for the discretization of strongly anistropic diffusion operators in magnetic fusion. *Computer Physics Communications*, 254:107375, 2020.

[27] X. Wang and L. Benabou. Numerical modeling of low-temperature and low-pressure sintering of silver microparticles based on surface and grain boundary diffusion mechanisms. *Mechanics of Advanced Materials and Structures*, 10 2020.

[28] S. Hazanov and M. Amieur. On overall properties of elastic heterogeneous bodies smaller than the representative volume. *International Journal of Engineering Science*, 33(9):1289 – 1301, 1995.

[29] S. Hazanov. Hill condition and overall properties of composites. 07 1998.

[30] S. Nemat-Nasser, N. Yu, and M. Hori. Bounds and estimates of overall moduli of composites with periodic microstructure. *Mechanics of Materials*, 15(3):163 – 181, 1993.

[31] P. M. Suquet. Introduction. In Enrique Sanchez-Palencia and André Zaoui, editors, *Homogenization Techniques for Composite Media*, pages 193–198, Berlin, Heidelberg, 1987. Springer Berlin Heidelberg.

[32] M. Ostoja-Starzewski. Material spatial randomness: from statistical to representative volume element. *Probabilistic Engineering Mechanics*, 21:112–132, 04 2006.

[33] L. Benabou and X. Wang. Simulation of silver nanoparticles sintering at high temperatures based on theoretical evaluations of surface and grain boundary mobilities. *International Journal for Computational Methods in Engineering Science and Mechanics*, 21(6):331–342, October 2020.